CHEMISTRY OF MATERIALS
Cite This: Chem. Mater. 2019, 31, 1597−1609
Article
pubs.acs.org/cm

Identification of Surface Structures in Pt_3Cr Intermetallic Nanocatalysts

Nicole J. LiBretto,[†] Ce Yang,[‡] Yang Ren,[§] Guanghui Zhang,*[,†,∥] and Jeffrey T. Miller*[,†]

[†]Davidson School of Chemical Engineering, Purdue University, 480 Stadium Mall Drive, West Lafayette, Indiana 47907, United States

[‡]Chemical Science and Engineering Division and [§]X-ray Science Division, Argonne National Laboratory, 9700 S. Cass Avenue, Lemont, Illinois 60439, United States

[∥]State Key Laboratory of Fine Chemicals, PSU-DUT Joint Center for Energy Research, School of Chemical Engineering, Dalian University of Technology, Dalian, Liaoning 116024, P. R. China

ABSTRACT: A precise understanding of the catalytic surface of nanoparticles is critical for relating their structure to activity. For silica-supported Pt−Cr bimetallic catalysts containing nominal Cr/Pt molar ratios of 0, 1.9, and 5.6, a fundamental difference in selectivity was observed as a function of composition for propane dehydrogenation, suggesting different surface structures. The formation of bimetallic catalysts and the phases present were confirmed by synchrotron in situ X-ray absorption spectroscopy (XAS) and X-ray diffraction (XRD) of the nanoparticle as a function of reduction temperature. With the increasing reduction temperature, there is a systematic increase in the Pt L_{III} edge X-ray absorption near edge structure (XANES) energy, which is consistent with the incorporation of more metallic Cr into the nanoparticles. Pt L_{III} edge extended X-ray absorption fine structure (EXAFS) shows that the nanoparticles are Pt rich regardless of the reduction temperature, and XRD shows the presence of both Pt and Pt_3Cr phases at temperatures below about 700 °C. For the latter, a full Pt_3Cr intermetallic alloy forms after reduction at 800 °C. This work also presents a method for the characterization of the catalytic surface by the analysis of XAS difference spectra and XRD difference patterns of the (reduced and oxidized) catalysts. The surface analysis suggests that Pt_3Cr formation begins at the surface, and at low reduction temperatures, a core−shell morphology is formed containing a Pt core with a Pt_3Cr surface. By combining the XAS and XRD analyses with transmission electron microscopy (TEM) particle sizes, the thickness of the shell can be approximated. All evidence indicates that the shell thickness increases with the increasing reduction temperature until a full alloy is formed after reduction at about 800 °C but only if there is enough Cr_2O_3 available near Pt nanoparticles to form Pt_3Cr. Catalysts containing a full monolayer coverage of Pt_3Cr have higher olefin selectivity (>97%) compared with partially covered Pt surfaces (88%).

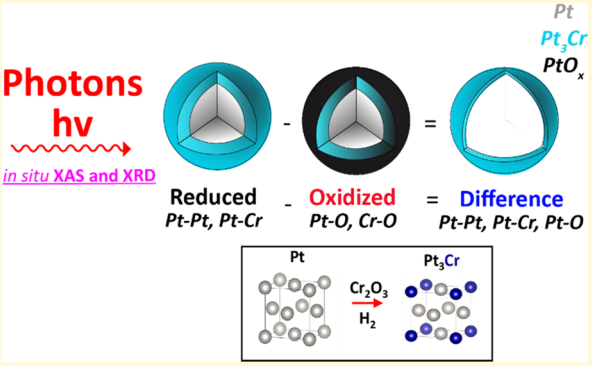

INTRODUCTION

Supported bimetallic nanoparticles are used in a large number of applications including heterogeneous catalysis, electrocatalysis, chemical sensing, and biomedicine.[1−4] As early as the 1970s, high-surface-area, highly dispersed bimetallic catalysts containing transition metals were investigated to understand how the combination of different metal pairs impacts catalytic performance.[5] Although it was clear in most cases that the combination of metals improves the catalytic behavior compared with the monometallic substituents, few characterizations were able to precisely identify the resulting structure and especially that of the catalytic surface. In recent years, improvements in nanoparticle synthesis to control the particle size and metal incorporation have led to a better understanding of the atomic order of nanoparticles.[6,7] For instance, core−shell structures, solid solutions, and intermetallic alloys, for which several structures may be possible, can be formed depending on the metal pairs and synthesis conditions. The difference among these structures is often subtle, especially in supported nanoparticles smaller than 5 nm in size.[8−10]

Determining the atomic distribution and alloy structures of supported bimetallic nanoparticles is challenging and requires a combination of techniques to identify the specific phases present.[11,12] For instance, X-ray absorption spectroscopy (XAS) has been used to determine whether a bimetallic phase is achieved, and the specific phases can be confirmed by in situ synchrotron X-ray diffraction (XRD).[8,9,13−17] The use of synchrotron radiation leads to a high signal-to-noise ratio in small nanoparticles of less than 2 nm and thus, it is possible to resolve the atomic order.[13] These characterizations, however, are not sufficient to determine the nanoparticles' surface

Received: November 15, 2018
Revised: February 1, 2019
Published: February 4, 2019

DOI: 10.1021/acs.chemmater.8b04774
Chem. Mater. 2019, 31, 1597−1609

structure, especially when it differs from the average composition. For example, surface segregation, or when the two metals de-alloy causing one to preferentially move to the surface, is possible. This could lead to changes in the surface compared to the average composition and structure, which has been reported for Pt−Au, where the alloy exhibited a Pt-rich alloy core with an Au-rich shell.[18] Alternatively, the core−shell nanoparticles may behave differently from full alloys of the same structure.[19,20] Identifying the surface composition and structure in bimetallic nanoparticles will lead to a better understanding of the catalytic performance; however, better methods for characterization of the surface are needed.

Here, we have prepared bimetallic Pt−Cr nanoparticle catalysts with a Pt_3Cr surface−Pt core structure, which are selective for propane dehydrogenation. The average structures were determined using in situ XRD and XAS analyses. In addition, a method is described to determine the surface structure composition, where the surface XAS and XRD were isolated using the difference spectrum of the reduced and oxidized spectra. This approach led to high resolution even in nanoparticles smaller than 2 nm. Through this difference analysis, identification of surface structures with resolution down to a single atomic layer are possible.

MATERIALS AND METHODS

Catalyst Preparation. Three Pt−Cr catalysts containing target weight loadings of 2 wt % Pt with 0, 1, and 3 wt % Cr were synthesized using sequential incipient wetness impregnation (IWI) so that the resulting catalysts contained Cr/Pt molar ratios of 0, 1.9, and 5.6, respectively. The samples were named according to their target weight loadings. Chromium nitrate nonahydrate [$Cr(NO_3)_3{\cdot}9H_2O$, Sigma-Aldrich] and citric acid (Sigma-Aldrich) were dissolved in 3 mL of Millipore water in a 1:1 molar ratio, and the resulting solution was added dropwise to 5 g of silica with grade 636 (pore size = 60 Å, surface area = 480 m^2/g). The obtained Cr/SiO_2 catalyst precursors were dried for 16 h at 125 °C and then calcined at 350 °C for 3 h. A second solution was made using 0.2 g of tetraamine platinum nitrate [$Pt(NH_3)_4(NO_3)_2$, Sigma-Aldrich] dissolved in 2 mL of Millipore water, and 1.75 mL of 30% ammonium hydroxide solution was added to adjust the pH to 11. The resulting solution was added dropwise to Cr/SiO_2 following the charge-enhanced dry impregnation method.[6] The Pt−Cr/SiO_2 catalysts were dried for 16 h at 125 °C and then calcined at 250 °C for 3 h. The catalysts were reduced in flowing H_2 at various temperatures from 250 to 800 °C to alter the degree of Cr incorporation.

Scanning Transmission Electron Microscopy (STEM). Catalysts were analyzed by STEM at the Center for Nanoscale Materials at the Argonne National Laboratory using an FEI Talos Scanning Transmission Electron Microscope (80−300 kV). The as-synthesized catalysts were prereduced at the desired reduction temperatures (250, 400, 550, 700, and 800 °C) using a ramp rate of 10 °C/min in H_2. Samples were dispersed in hexane and deposited on an Au-coated holey carbon grid (TedPella). Images were taken using a high-angle annular dark-field detector at 300 kV. The measurements were performed on the samples after they were exposed to air, which is not expected to change the particle size distribution. The average particle size was determined by performing a statistical distribution analysis on a sample size of 250−300 particles imaged using ImageJ particle size counting software.[21]

In Situ X-Ray Absorption Spectroscopy (XAS). In situ XAS experiments were performed at the 10-BM-B beamline at the Advanced Photon Source (APS), Argonne National Laboratory, at the Pt L_{III} (11.564 keV) edge in transmission mode, with an energy resolution of 0.3 eV and edge energy precision greater than 0.1 eV. $2Pt/SiO_2$, $2Pt1Cr/SiO_2$, and $2Pt3Cr/SiO_2$ were ground into a powder, pressed into a sample holder, and sealed in a sample cell with leak-tight Kapton end caps. The sample cell was treated with 3.5% H_2/He for 30 min at 250, 400, 550, 700, and 800 °C sequentially. The cell was cooled to room temperature in flowing He between each temperature exposure, sealed, and moved to the beamline to acquire data. The He tank was connected to a gas purifier to reduce the possibility of O_2 exposure. A 1 nm Pt/SiO_2 sample was used for reference to verify that the cell was not accidentally exposed to O_2 in between the H_2 pretreatment and scanning. After H_2 treatment at each temperature, the sample cell was purged with 20% O_2 at room temperature for 15 min to allow for surface oxidation of the nanoparticles, and a second spectrum was recorded.[22] Each measurement was accompanied by simultaneous measurement of a Pt foil scan obtained through a third ion chamber for internal energy calibration.

All data were analyzed using WinXAS 3.1 software[23] using standard fitting procedures to find the coordination number and bond distances between Pt and its neighbors. Extended X-ray absorption fine structure (EXAFS) was obtained using a least-squared fit in r-space performed on isolated k^2-weighted Fourier transform data. The data were fit using the experimental Pt−Pt phase and amplitude files obtained from a Pt foil. The theoretical Pt−Cr phase and amplitude files were obtained from FEFF6[24] calculations. Each sample was fit using two scattering paths (Pt−Pt and Pt−Cr).

Difference XAS analysis was used to determine the surface composition of the nanoparticles. First, spectra were recorded after reducing the samples at varying temperatures in H_2. Then, the samples were subsequently oxidized by exposure to air at room temperature and scanned again. The difference in k^0-weighted χ's (reduced−oxidized) was used to show changes in the surface. The resulting difference chi spectrum, representing the surface of the nanoparticles, was then k^2-weighted, and a Fourier transform was fit. The data was fit using three scattering paths (Pt−Pt, Pt−Cr, and Pt−O). An experimental phase and amplitude were obtained for Pt−O using PtO as a reference compound. The phase of the Pt−O scattering pair was π-radians out of phase from the normal EXAFS. The Pt−O amplitude was unchanged.

In Situ X-ray Diffraction (XRD). In situ XRD measurements were performed at the 11-ID-C beamline at the APS, using X-rays of λ = 0.1173 Å (105.715 keV), and data was acquired using a PerkinElmer large-area detector. The high-energy and high-flux X-rays are necessary for collecting diffraction patterns on nanoparticles less than 10 nm in size to increase the signal-to-noise ratio and reduce the background from the SiO_2 support. Samples were pressed into a self-supported pellet (<2 mm thickness) and then loaded into a thermal stage. The cell was purged with He before a flow of 3.5% H_2/He at 100 ccm was introduced, and the temperature was increased to the target temperature (250, 400, 550, 700, and 800 °C). After diffraction measurements were completed at the reduction temperature, the cell was cooled to 35 °C and a second diffraction measurement was obtained. A third set of diffraction measurements was obtained at room temperature for each sample after being exposed to room-temperature air, post reduction.

The background scattering of the empty cell and silica was obtained under the same conditions and subtracted from the XRD pattern. The diffraction patterns were collected as 2-D Scherrer rings and were integrated using Fit2D software[25] to obtain 1-D diffraction patterns as scattering intensity versus 2θ plots. Theoretical diffraction patterns for possible Pt and Pt−Cr structures were simulated at room temperature using crystal information files imported to Materials Analysis Using Diffraction[26] and were used to identify the catalyst phase. All diffraction patterns were used to obtain the unit cell size and Pt−Pt and Pt−Cr bond distances. The nanoparticle size (d) was calculated using the Scherrer equation $\left(d = \frac{\lambda}{\beta \cos\theta}\right)$, where λ is the X-ray wavelength, β is the full width at half-maximum, a peak broadening parameter, and θ is the Bragg angle. Bragg's law $\left(d_{111} = \frac{\lambda}{\sin\theta}\right)$ was used to find the lattice spacing (d_{111}) of the nanoparticle, and then the lattice constant (a) was calculated using the geometry of the (111) plane $\left({d_{111}}^2 = \frac{a^2}{\sqrt{3}}\right)$. The Pt−Pt and Pt−

DOI: 10.1021/acs.chemmater.8b04774
Chem. Mater. 2019, 31, 1597−1609

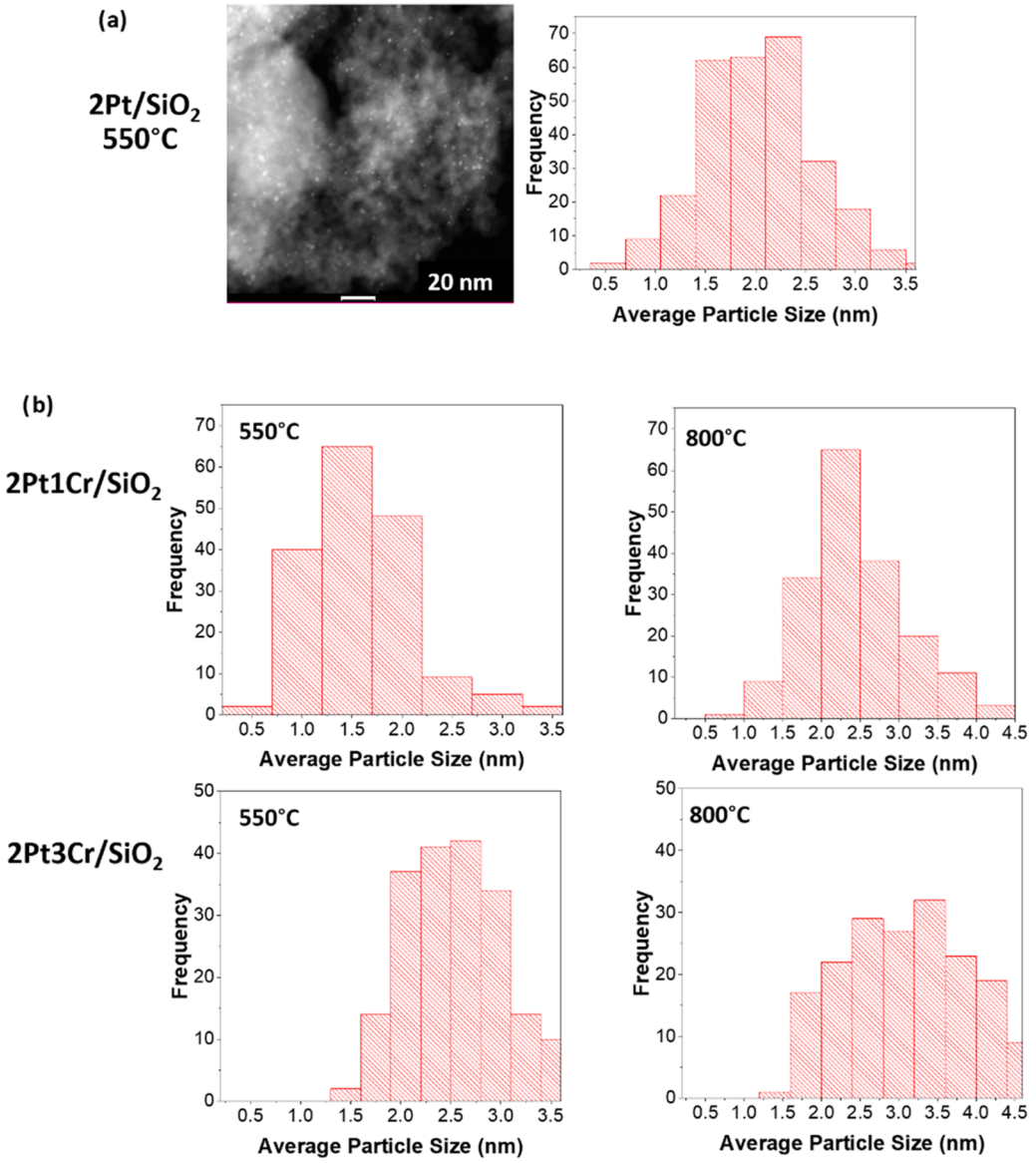

Figure 1. (a) STEM image and particle size distribution for $2Pt/SiO_2$ after reduction at 550 °C. (b) Particle size distributions for $2Pt1Cr/SiO_2$ and $2Pt3Cr/SiO_2$ after reduction at 550 °C and 800 °C.

Cr bond distances were calculated from the obtained lattice parameter.

Catalyst Performance Evaluation. Propane dehydrogenation was used to indicate structural changes to monometallic Pt with the addition of Cr to form bimetallic catalysts of different morphologies. Catalyst performance tests were performed at 550 °C in a fixed bed reactor with a quartz reactor tube of 3/8 in. OD. The weight of the catalyst (particle size 250−500 μm) loaded into the reactor ranged from 25 to 500 mg to vary the initial propane conversion and was diluted with silica to reach a total of 1 g. A thermocouple was used to measure the temperature in the center of the bed. Before each test, the catalyst was reduced for 30 min at a minimum temperature of 550 °C under 100 ccm 5% H_2/N_2 and then cooled down to the target reaction temperature (550 °C). Catalysts reduced at temperatures lower than the reaction temperature were not evaluated for their performance due to changes in structure at higher temperatures. The reaction was performed in 2.5% C_3H_8 and 2.5% H_2 and balanced with N_2. The products were analyzed with a Hewlett Packard 6890 Series gas chromatograph using a flame ionization detector with a Restek Rt-Alumina BOND/Na_2SO_4 GC column (30 m in length, 0.32 mm ID, and 0.5 μm film thickness).

RESULTS

STEM. Catalysts containing loadings of 2 wt % Pt ($2Pt/SiO_2$) with 1 wt % Cr ($2Pt1Cr/SiO_2$) and 3 wt % Cr ($2Pt3Cr/SiO_2$) were prepared by the pH-modified impregnation method.[6] The catalysts were reduced at various temperatures starting as low as 250 °C up to 800 °C. A representative STEM image and particle size distribution are shown for $2Pt/SiO_2$ after reduction at 550 °C (Figure 1a). STEM particle size distributions are shown for the Cr-containing catalysts reduced at 550 and 800 °C, which show slightly larger particle sizes after reduction at higher temperatures (Figure 1b). In each instance, there is a narrow particle size distribution of uniform, small sized nanoparticles, similar to that of previous catalysts prepared by this synthesis method.[6] Upon increasing the reduction temperature, the averaged particle size of $2Pt3Cr/SiO_2$ increased from 2.5 to 3.3 nm, whereas for $2Pt1Cr/SiO_2$, the particle size increased from 1.9 to 2.4 nm. STEM indicates the presence of few particles larger than 5 nm in both 2Pt1Cr/

DOI: 10.1021/acs.chemmater.8b04774
Chem. Mater. 2019, 31, 1597−1609

SiO_2 and 2Pt3Cr/SiO_2 after reduction at 800 °C. The particle sizes are summarized in Table 1.

Table 1. Average Particle Sizes of Pt−Cr Catalysts Compared with Those of Monometallic Pt

	reduction temperature (°C)	average particle size (nm)
2Pt/SiO_2	550	1.9
2Pt1Cr/SiO_2	550	1.9
	800	2.4
2Pt3Cr/SiO_2	550	2.5
	800	3.3

In Situ XAS. The local geometry of the reduced Pt at various stages of particle growth was determined by performing in situ XAS at the Pt L_{III} edge. The change in the energy and shape of the X-ray absorption near edge structure (XANES) is characteristic of a change in the Pt coordination environment. Shifts to higher energies are observed in 2Pt3Cr/SiO_2 with increasing reduction temperature and are consistent with increasing amounts of metallic Cr in the nanoparticles (Figure 2), as also evidenced in the EXAFS described below.

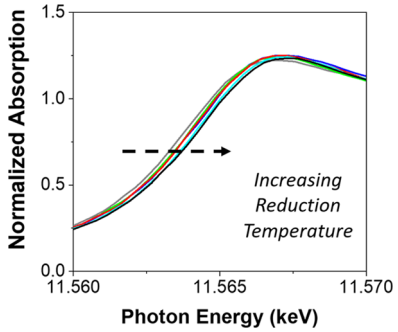

Figure 2. Pt L_{III} edge normalized XANES of 2Pt3Cr/SiO_2 after reduction at 250 °C (blue), 400 °C (green), 550 °C (red), 700 °C (light blue), and 800 °C (black) in flowing H_2 compared with that of 2Pt/SiO_2 reduced at 550 °C (gray).

A XANES energy shift of 0.1 eV was observed after reduction at 250 °C, presumably due to the incorporation of some reduced Cr. The XANES energy of 2Pt3Cr/SiO_2 increased by 0.3 and 0.6 eV as the catalyst was reduced at 550 and 800 °C, respectively. Larger XANES energy shifts are observed in 2Pt3Cr/SiO_2 than in 2Pt1Cr/SiO_2 at the same reduction temperatures (Figure 3), which suggests that the amount of CrO_x available to form bimetallic nanoparticles plays a role in the resulting nanoparticle composition. For instance, after reduction at 800 °C, the XANES energy shifts from 11.5640 keV in monometallic Pt to 11.5644 keV in 2Pt1Cr/SiO_2 and 11.5646 keV in 2Pt3Cr/SiO_2.

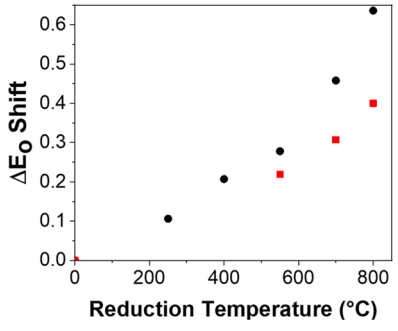

Figure 3. Change in XANES energy shift compared with Pt (11.5640 keV) as a function of reduction temperature for 2Pt1Cr/SiO_2 (red) and 2Pt3Cr/SiO_2 (black).

Evidence for the formation of bimetallic nanoparticles was obtained by EXAFS (Figure 4), which confirmed the presence of Pt−Cr scatters. The shape of the Fourier transforms, representing scattering from Pt neighbors, demonstrates a changing peak ratio in Pt−Cr catalysts after reduction at increasing temperatures. The magnitude of the Fourier transform (Figure 4a) shows an increased intensity of the first peak at ∼1.8 Å and a decreased intensity of the third peak at ∼2.8 Å compared with monometallic Pt with increasing reduction temperature to 800 °C, where the intensities of both peaks are about the same. The addition of Cr also changes the imaginary part of the Fourier transform of 2Pt3Cr/SiO_2, consistent with the addition of different ratios of metallic Cr (Figure 4b).

The EXAFS data were fit to determine the Pt−Pt (CN_{Pt-Pt}) and Pt−Cr (CN_{Pt-Cr}) coordination numbers and bond distances (Table 2). After reduction at 550 °C, 2Pt1Cr/SiO_2 has a CN_{Pt-Pt} of 8.0 and a CN_{Pt-Cr} of 2.2 or a ratio of Pt−Cr to Pt−Pt neighbors of 0.28. Thus, the nanoparticle are Pt rich. As the reduction temperature increases to 700 and 800 °C, the ratio increases to 0.38, and although the nanoparticles are still Pt rich, at higher reduction temperatures, the Cr content of the bimetallic nanoparticles increases. The average Pt−Pt (R_{Pt-Pt} = 2.73 Å) and Pt−Cr (R_{Pt-Cr} = 2.70 Å) bond distances in 2Pt1Cr/SiO_2 are nearly constant at all reduction temperatures (Table 2).

Similar results were observed for 2Pt3Cr/SiO_2. After reduction at 250 °C, the CN_{Pt-Cr}/CN_{Pt-Pt} is 0.16 and the nanoparticle are Pt rich. The CN_{Pt-Cr}/CN_{Pt-Pt} ratio increases to 0.25 and 0.50 after reduction at 550 and 800 °C, respectively. The average bond distances in 2Pt3Cr/SiO_2 are very similar to those in 2Pt1Cr/SiO_2 (Table 2).

In both catalysts, a simultaneous increase in CN_{Pt-Cr} and a decrease in CN_{Pt-Pt} is observed with the increasing reduction temperature. Reduction at 550 °C leads to very similar coordination geometries in 2Pt1Cr/SiO_2 and 2Pt3Cr/SiO_2. Both catalysts are Pt rich, where the average CN_{Pt-Cr}/CN_{Pt-Pt} is about 0.30. As the reduction temperature is increased to 800 °C, 2Pt3Cr/SiO_2 (CN_{Pt-Cr}/CN_{Pt-Pt} = 0.52) is slightly more Cr rich than 2Pt1Cr/SiO_2 (CN_{Pt-Cr}/CN_{Pt-Pt} = 0.38), consistent with a slightly larger XANES energy shift in the former. The larger amount of Cr incorporation in 2Pt3Cr/SiO_2 is likely due to higher Cr loading.

In Situ XRD. Although XAS indicates the formation of bimetallic nanoparticles, in situ synchrotron XRD was performed to identify the resulting bimetallic phase. The X-ray energy was 105.715 keV resulting in diffraction patterns at a low 2θ angle, e.g., of less than about 8°, compared with laboratory XRD. The high flux of the synchrotron XRD gives a better signal-to-noise ratio, and the high-energy X-rays allow for increased sensitivity for heavy scatters, for example, Pt nanoparticles compared to SiO_2. Finally, the large-area detector can be moved to a long distance from the sample to allow for better spatial resolution of closely spaced reflections from different phases.[27] After reduction at temperatures below 550 °C, the small nanoparticles (<3 nm) have broad diffraction peaks, and the features are difficult to resolve. In the diffraction pattern of monometallic Pt nanoparticles

DOI: 10.1021/acs.chemmater.8b04774
Chem. Mater. 2019, 31, 1597−1609

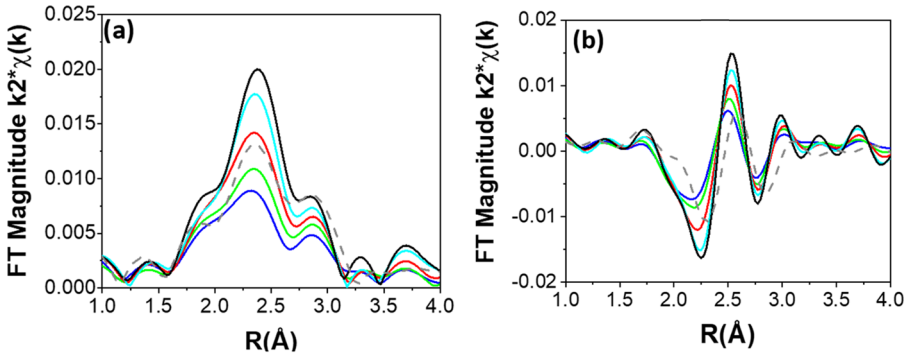

Figure 4. Pt L_{III} edge EXAFS (a) magnitude and (b) imaginary part for 2Pt3Cr/SiO_2 after reduction at 250 °C (blue), 400 °C (green), 550 °C (red), 700 °C (light blue), and 800 °C (black) in flowing H_2 compared with that for 2Pt/SiO_2 reduced at 550 °C (gray dashed).

Table 2. Pt L_{III} Edge XAS Fitting Parameters for 2Pt1Cr/SiO_2 and 2Pt3Cr/SiO_2 after Reduction in H_2 at Successively Increasing Temperatures

sample	reduction temperature (°C)	XANES energy (keV)	scattering path	CN	R (Å)	$\Delta\sigma^2$ (Å^2)	ΔE_o (eV)
2Pt/SiO_2	550	11.5640	Pt−Pt	10.2	2.76	0.003	−0.4
2Pt1Cr/SiO_2	550	11.5643	Pt−Pt	8.0	2.73	0.004	−1.3
			Pt−Cr	2.2	2.70	0.003	0.9
	700	11.5643	Pt−Pt	8.3	2.73	0.004	−1.3
			Pt−Cr	2.9	2.70	0.003	0.0
	800	11.5644	Pt−Pt	8.4	2.73	0.004	−1.6
			Pt−Cr	3.2	2.71	0.003	−1.6
2Pt3Cr/SiO_2	250	11.5641	Pt−Pt	7.5	2.75	0.006	−0.2
			Pt−Cr	1.2	2.69	0.003	0.7
	400	11.5642	Pt−Pt	8.0	2.74	0.005	−0.2
			Pt−Cr	1.9	2.69	0.003	−1.5
	550	11.5643	Pt−Pt	8.1	2.73	0.004	−1.6
			Pt−Cr	2.4	2.70	0.003	1.1
	700	11.5645	Pt−Pt	7.8	2.73	0.003	−0.8
			Pt−Cr	3.6	2.70	0.003	1.1
	800	11.5646	Pt−Pt	7.9	2.73	0.003	0.5
			Pt−Cr	4.1	2.73	0.003	2.1

(face centered cubic (FCC) crystal structure), there are four main reflections representing the (111), (200), (220), and (311) planes. With the increasing particle size, monometallic Pt results in a slight shift in reflection to slightly lower 2θ values due to longer bond distances.[28,29] Simulations for known bulk phase Pt−Cr phases (Pt_3Cr, PtCr, and $PtCr_3$) at room temperature are compared with the diffraction patterns of the bimetallic catalysts (Figure 5).[30] Each catalyst's

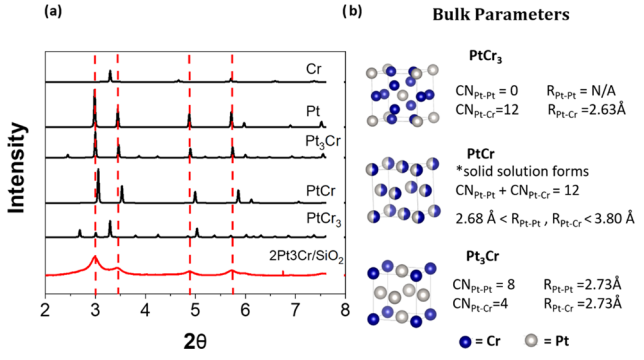

Figure 5. (a) XRD of 2Pt3Cr/SiO_2 reduced at 550 °C compared with simulations of Pt−Cr alloy structures (X-ray energy = 105.715 keV). (b) Unit cells and bulk parameters of possible Pt−Cr phases.

diffraction patterns at elevated temperatures of reduction and after cooling to room temperature were nearly identical. Data is reported at room temperature, where there is less thermal strain. The bimetallic catalysts' diffraction patterns do not match those for the PtCr or $PtCr_3$ phases. However, the near proximity of monometallic Pt and Pt_3Cr reflection positions make it difficult to distinguish between the two phases in small nanoparticles. The shifts in the diffraction could also possibly be due to the formation of a Pt−Cr randomly ordered solid solution (containing Pt and Cr atoms). Solid solutions typically occur in metals that have the same crystal structure; however, Cr has a BCC structure and Pt is FCC. The Pt−Cr phase diagram indicates that Cr is insoluble in Pt.[30] Finally, increasing amounts of Cr, which are observed by EXAFS, would lead to increasing shifts to higher 2θ in the diffraction patterns, which is not observed. If there were a solid solution between Pt and Cr with compositions from 10 to 33%, for example, larger shifts in the diffraction patterns would have occurred and been easily resolved from Pt. The constant position of diffraction peaks with the increasing Cr composition is a characteristic of two phases and not of a solid solution.

After reduction at 250, 400, and 550 °C, the diffraction patterns are broad, spanning over both Pt and Pt_3Cr simulation positions (Figure 6a). The nanoparticles formed after reduction at low temperatures (<550 °C) are similar to Pt,

DOI: 10.1021/acs.chemmater.8b04774
Chem. Mater. 2019, 31, 1597−1609

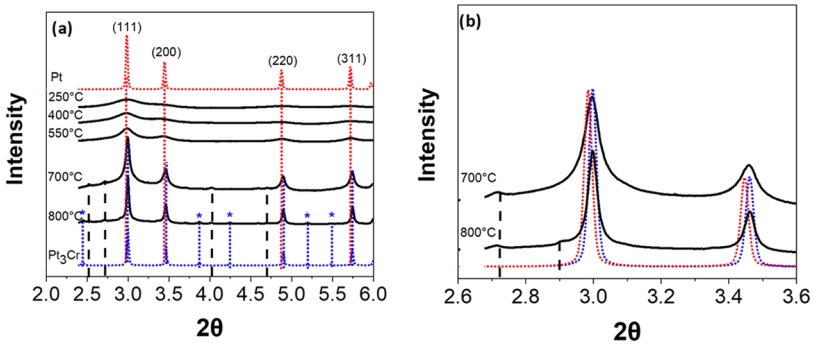

Figure 6. (a) XRD patterns for 2Pt3Cr/SiO_2 as the reduction temperature increases compared with simulations for Pt (red dotted) and Pt_3Cr (blue dotted) with blue * representing superlattice diffraction peaks and guidelines for Cr_2O_3 (black dashed). (b) XRD pattern corresponding to the (111) and (200) planes for 2Pt3Cr/SiO_2 after reduction at 700 and 800 °C.

Table 3. Particle Size and Lattice Parameter Calculated from the (111) Plane of Experimental XRD Patterns

sample	reduction temperature (°C)	d_{XRD} (nm)	a (Å)	R_{Pt-Pt} (Å)	reflections (2θ, deg)
2Pt/SiO_2	550	1.8	3.91	2.77	2.957, 3.396, 4.852, 5.702
	700	2.1	3.92	2.77	2.969, 3.146, 4.844, 5.702
2Pt1Cr/SiO_2	550	4.3	3.89	2.73	2.999, 3.460, 4.897, 5.749
	700	10.3	3.88	2.73	2.997, 3.460, 4.897, 5.749
2Pt3Cr/SiO_2	250	1.5	3.89	2.75	2.978, 3.452, 4.871, 5.717
	400	1.8	3.90	2.74	2.978, 3.441, 4.882, 5.740
	550	3.2	3.90	2.74	2.978, 3.447, 4.882, 5.740
	700	12.3	3.88	2.73	2.997, 3.460, 4.895, 5.742
	800	18.1	3.87	2.73	2.997, 3.462, 4.897, 5.745

but the EXAFS indicates that some Cr is present. As the Cr content increases, the Pt reflections decrease slightly, whereas the reflections for Pt_3Cr increase slightly. The reflections from the two very similar diffraction patterns change in shape with the increasing Cr content, but not in position, suggesting increasing amounts of the ordered Pt_3Cr phase.

To confirm the Pt_3Cr nanoparticle structure, 2Pt3Cr/SiO_2 was reduced at higher temperatures (700 and 800 °C) to produce a full alloy. At the higher reduction temperature, the particles also were slightly larger (increasing from 2.5 to 3.3 nm) with increased intensities and narrower peaks. These slightly larger particles also result in superlattice diffraction peaks or features corresponding to lower-symmetry crystal planes. The diffraction patterns obtained after reduction at higher temperatures are shown in Figure 6b. Although reflections are larger after reduction at 700 °C, Pt and Pt_3Cr still cannot be resolved due to the close peak proximity. The increasing reduction temperature also led to additional reflections that match the diffraction pattern for Cr_2O_3 (black dashed guidelines). After reduction at 800 °C, the larger diffraction peaks (Table 3) and the smaller superlattice diffraction peaks were observed at 2.45, 3.87, 4.24, 5.20, and 5.48° (indicated by *), which confirms the formation of the Pt_3Cr structure.[31]

With the increasing reduction temperature, the lattice parameter changes with slight changes in particle size and composition (Table 3). Particles less than 3 nm in size typically have shorter bond distances, which lead to a slight lattice parameter contraction.[32] In addition, because Cr is a smaller element than Pt, a structure formed between these two atoms also decreases the size of the unit cell compared with Pt. Pt nanoparticles have a lattice parameter, a, of 3.91 Å. An increase in the size of Pt nanoparticles results in lattice parameter expansion to slightly larger values ($a_{bulk\ Pt}$ = 3.92 Å), whereas the addition of Cr reduces the lattice parameter of monometallic Pt ($a_{bulk\ Pt3Cr}$ = 3.87 Å). The lattice parameter of 2Pt3Cr/SiO_2 increased from 3.89 Å after reduction at 250 °C to 3.90 Å at 400 and 550 °C. The EXAFS indicates that the nanoparticles have increasing amounts of metallic Cr, which should lead to a decreased lattice parameter; however, the lattice parameter increases slightly, likely due to the increase in the particle size and the low Cr levels in the nanoparticles. When the nanoparticles are reduced at 700 and 800 °C, although the particles continue to increase slightly in size, the lattice parameter decreases to 3.88 and 3.87 Å, respectively, consistent with the formation of Pt_3Cr.

In summary, at lower reduction temperatures, the diffraction patterns are shifted slightly to higher 2θ, i.e., smaller lattice parameter, due to the incorporation of Cr into the bimetallic nanoparticle. Although the reflections are broad and asymmetric and the peaks from Pt and Pt_3Cr cannot be resolved, the reflection positions and peak shapes are consistent in these two phases. At the reduction of 800 °C, Pt_3Cr intermetallic alloy formation is confirmed by XRD. The XRD patterns of 2Pt1Cr/SiO_2 are also very similar to those of 2Pt3Cr/SiO_2, although the full Pt_3Cr alloy does not form on the former even after reduction at 800 °C. Thus, 2Pr1Cr/SiO_2 forms two phases at all reduction temperatures, consistent with the higher Pt−Pt coordination in the EXAFS compared with 2Pt3Cr/SiO_2.

Catalyst Evaluation: Propane Dehydrogenation. The catalytic performances of 2Pt1Cr/SiO_2 and 2Pt3Cr/SiO_2 for propane dehydrogenation were compared with that of monometallic Pt. Because catalysis is a surface phenomenon, any change in the surface composition and structure will result in a different performance. The conversion and selectivity were determined for propane dehydrogenation with 2.5% C_3H_8, 2.5% H_2 with balanced N_2 at 550 °C after the catalysts were

DOI: 10.1021/acs.chemmater.8b04774
Chem. Mater. 2019, 31, 1597−1609

prereduced at 550 and 800 °C. The catalysts were evaluated in the presence of H_2 since increased hydrogen-to-hydrocarbon ratio increases the probability for hydrogenolysis and is, therefore, a more rigorous test for the dehydrogenation selectivity. Under these conditions, propane is predominately converted to propylene but methane, ethane, and ethylene are also formed. The carbon balance for these tests was approximately 100%.

The initial propylene selectivity of the catalysts was compared over a range of conversions up to about 40% (Figure 7). For 2Pt/SiO_2 reduced at 550 °C (1.9 nm), at about

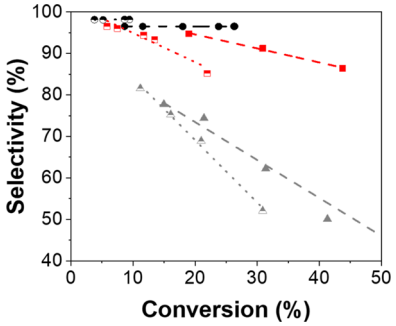

Figure 7. Initial selectivity for Pt−Cr catalysts containing 1 wt % Cr (red) and 3 wt % Cr (black) in C_3H_8 dehydrogenation reactions after reduction at 550 °C (full) and 800 °C (half-full) compared with that for monometallic Pt (gray) with linear fit lines (dashed) in 2.5% C_3H_8, 2.5% H_2 with balanced N_2.

10% propane conversion, the propylene selectivity was near 80%. The selectivity decreases rapidly with the increasing conversion; for example, the propylene selectivity was about 50% at 40% propane conversion. Reduction of 2Pt/SiO_2 at 800 °C leads to lower selectivity, especially for propane conversions over about 20%. For 2Pt1Cr/SiO_2 reduced at 500 °C (1.9 nm) and 800 °C (2.4 nm), the selectivity at any conversion is significantly improved compared with that for monometallic Pt. However, like that of 2Pt/SiO_2, the resulting olefin selectivity decreases with the increasing conversion.

On the other hand, very high olefin selectivity (98%) is obtained at all conversions for 2Pt3Cr/SiO_2 reduced at 500 °C (2.7 nm) and 800 °C (3.3 nm) (Table 4). The difference in catalyst selectivities implies that 2Pt1Cr/SiO_2 and 2Pt3Cr/SiO_2 have different surface compositions, despite their similar EXAFS and XRD characterizations.

Industrially, both Pt and CrO_x are known dehydrogenation catalysts.[33−35] The rates per gram of Pt (or per g Cr for Cr/SiO_2 catalysts) are reported in Table 4. The rates of Pt are significantly higher than those of Cr oxide, implying that Pt is the active site. H_2−O_2 titration is a standard way to determine the fraction of surface Pt. Since these catalysts also contain Cr_2O_3, which can also be oxidized, this method is unreliable for these catalysts. However, the fraction of oxidized Pt can be determined by XAS, and the Pt−O coordination number can be used to estimate the dispersion and calculate a turnover rate (TOR).

The Pt−O coordination numbers obtained from the oxidized catalysts are given in Table 5. Fully oxidized Pt nanoparticles have a CN_{Pt-O} = 4; thus, the dispersion is obtained by dividing the oxidized catalyst's Pt−O coordination number by 4. This method works well for small nanoparticles with a high fraction of surface atoms but becomes less reliable at sizes above about 6−8 nm where the Pt−O coordination number is small. The Pt dispersions are also given in Table 5. The TORs of the bimetallic Pt−Cr catalysts are very similar to those of monometallic Pt (Table 5), suggesting that Pt is the active site in the Pt_3Cr alloy and that the TOR of monometallic Pt is not much different from that of the Pt_3Cr alloy. The TOR of Pt_3Cr is also very similar to those reported for other intermetallic Pt alloys.[9,14−16,19]

DISCUSSION

Formation of Pt−Cr bimetallic nanoparticles on carbon electrocatalysts has previously been reported by Antolini et al.[31] Although improved ORR performance was observed with the addition of Cr, this was not correlated to alloy formation. Rather, the activity was suggested to be due to the presence of Cr oxides. Similarly, Cui et al.[36] studied Pt−Cr/C for ORR reactions as a function of annealing temperature. It was also suggested that the Pt_3Cr phase was formed but only after treatment at 600 °C.

In this study, the combination of XAS and XRD indicated that at reduction temperatures below about 700 °C, the nanoparticles contain two phases (Pt and Pt_3Cr). Although both 2Pt1Cr/SiO_2 and 2Pt3Cr/SiO_2 form bimetallic catalysts with similar average compositions and structures, the differences in catalytic selectivity indicate that the surface compositions are not equivalent. To quantify these differences, a surface-sensitive characterization is needed. Surface oxidation of the nanoparticles was used to determine the Pt dispersion. However, Cr was also oxidized as evidenced by the loss of Pt−Cr coordination.[37] Since the metallic bonds of the oxidized nanoparticles are identical to those of the particle interior of the reduced sample, the difference spectrum represents the bonds only from the surface. For EXAFS, in this difference spectrum (reduced minus oxidized), there are surface Pt−Pt, Pt−Cr, and Pt−O scatters. This is shown schematically in Figure 8. In the difference fit, since the oxidized catalysts are

Table 4. C_3H_8 Dehydrogenation Performed at 550 °C in 2.5% C_3H_8, 2.5% H_2 Balanced in N_2

	reduction temperature (°C)	$S_{C_3H_6}$ (%) at 20% conversion	rate (mol $C_3H_6/g_{cat}/s$)	Pt dispersion[b]	TOR (1/s)	phases present
2Pt/SiO_2	550	74	1.5×10^{-5}	0.20	0.3	Pt
	800	70	2.1×10^{-6}	0.15	0.1	
2Pt1Cr/SiO_2	550	95	3.3×10^{-5}	0.20	0.4	Pt, Pt_3Cr
	800	88	1.8×10^{-6}	0.15	0.1	
2Pt3Cr/SiO_2	550	98	8.4×10^{-5}	0.18	0.3	Pt, Pt_3Cr
	800	98	1.8×10^{-6}	0.10	0.2	Pt_3Cr
1Cr/SiO_2[a]	550	97	8.0×10^{-7}			CrO_x
3Cr/SiO_2[a]	550	98	2.6×10^{-7}			

[a]Selectivity reported at 5% conversion. [b]Pt dispersion was determined using the Pt−O coordination number of the oxidized XAS spectra.

DOI: 10.1021/acs.chemmater.8b04774
Chem. Mater. 2019, 31, 1597−1609

Table 5. XAS Fitting Parameters for Oxidized 2Pt1Cr/SiO_2 and 2Pt3Cr/SiO_2 Post Reduction in H_2

sample	reduction temperature (°C)	scattering path	CN	R (Å)	$\Delta\sigma^2$ (Å^2)	ΔE_o (eV)	Pt dispersion
2Pt1Cr/SiO_2	550	Pt−Pt	6.5	2.73	0.004	−0.9	0.20
		Pt−Cr	1.6	2.70	0.003	0.9	
		Pt−O	0.8	2.05	0.001	0.7	
	700	Pt−Pt	7.5	2.73	0.004	1.4	0.15
		Pt−Cr	2.3	2.70	0.003	−2.0	
		Pt−O	0.6	2.05	0.001	1.6	
	800	Pt−Pt	7.9	2.73	0.004	1.3	0.15
		Pt−Cr	3.3	2.71	0.003	−1.5	
		Pt−O	0.6	2.05	0.001	1.8	
2Pt3Cr/SiO_2	250	Pt−Pt	5.8	2.73	0.006	1.4	0.23
		Pt−Cr	0.6	2.69	0.003	2.0	
		Pt−O	0.9	2.05	0.001	−0.7	
	400	Pt−Pt	6.5	2.74	0.005	0.1	0.20
		Pt−Cr	0.9	2.69	0.003	−2.8	
		Pt−O	0.8	2.05	0.001	0.7	
	550	Pt−Pt	7.9	2.75	0.004	1.3	0.18
		Pt−Cr	1.8	2.69	0.003	−6.2	
		Pt−O	0.7	2.05	0.001	3.0	
	700	Pt−Pt	7.4	2.73	0.003	−1.8	0.15
		Pt−Cr	3.2	2.73	0.003	1.0	
		Pt−O	0.6	2.05	0.001	6.3	
	800	Pt−Pt	7.9	2.73	0.003	−2.0	0.10
		Pt−Cr	3.9	2.73	0.003	−2.0	
		Pt−O	0.4	2.05	0.001	0.8	

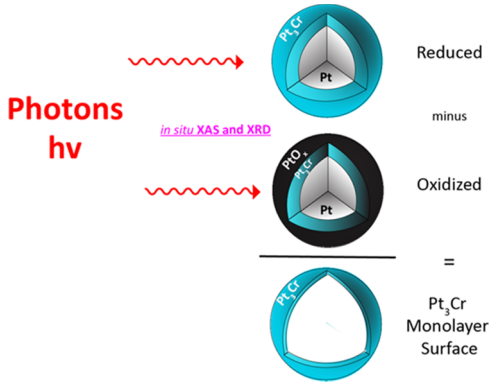

Figure 8. Approach for difference analysis, where reduced Pt−Cr nanoparticles are subsequently oxidized, and the raw data is subtracted to isolate the nonoxidized surface.

subtracted from the reduced spectrum, the Pt−O scattering path is π-radians out of phase from a normal scattering pair, i.e., a direct EXAFS fit.

The reduced and oxidized magnitudes and imaginary parts for the 2Pt3Cr/SiO_2 catalysts are shown in Figure 9a. The small difference represents the loss of metallic peaks upon oxidation and formation of Pt−O bonds. The difference EXAFS is shown in Figure 9b. Since the metallic peaks that are common to both the reduced and oxidized nanoparticles are removed in the difference spectrum, the surface Pt−O and surface Pt−Pt and Pt−Cr are more easily resolved and analyzed. The fits of the difference EXAFS are given in Table 6. The Pt−O coordination numbers in the difference fit are consistent with those in the oxidized catalyst. For 2Pt3Cr/SiO_2, reduction at 250 °C gives a surface CN_{Pt-Cr}/CN_{Pt-Pt} ratio of 0.31, which is higher than that of the reduced catalyst, 0.16, indicating that the surface is more Cr rich than the average composition. Also, in a Pt_3Cr alloy, CN_{Pt-Cr}/CN_{Pt-Pt} = 0.5; thus, reduction at 250 °C does not lead to a full Pt_3Cr

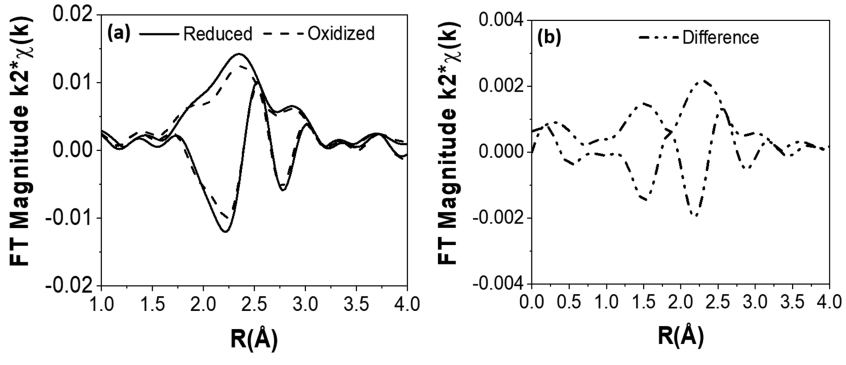

Figure 9. 2Pt3Cr/SiO_2 after reduction at 550 °C: (a) Fourier transform magnitudes and imaginary components of the reduced and oxidized catalysts. (b) Difference EXAFS.

DOI: 10.1021/acs.chemmater.8b04774
Chem. Mater. 2019, 31, 1597−1609

Table 6. Difference XAS Fitting Parameters for the Surface Compositions of $2Pt1Cr/SiO_2$ and $2Pt3Cr/SiO_2$

sample	reduction temperature (°C)	scattering path	CN	R (Å)	$\Delta\sigma^2$ (Å^2)	ΔE_o (eV)	Pt dispersion
$2Pt1Cr/SiO_2$	550	Pt−Pt	1.5	2.75	0.003	−1.0	0.16
		Pt−Cr	0.6	2.71	0.003	3.8	
		Pt−O	0.4	2.05	0.001	−3.5	
	700	Pt−Pt	1.5	2.75	0.003	−2.9	0.13
		Pt−Cr	0.6	2.68	0.003	−2.8	
		Pt−O	0.3	2.05	0.001	−4.3	
$2Pt3Cr/SiO_2$	250	Pt−Pt	1.6	2.74	0.003	2.1	0.22
		Pt−Cr	0.5	2.73	0.003	6.3	
		Pt−O	0.6	2.05	0.001	−2.5	
	400	Pt−Pt	1.1	2.73	0.003	0.9	0.20
		Pt−Cr	0.5	2.73	0.003	5.6	
		Pt−O	0.4	2.05	0.001	−1.7	
	550	Pt−Pt	0.9	2.73	0.003	−4.0	0.18
		Pt−Cr	0.5	2.73	0.003	5.1	
		Pt−O	0.3	2.05	0.001	−2.7	
	700	Pt−Pt	0.7	2.73	0.003	−0.3	0.14
		Pt−Cr	0.5	2.73	0.003	2.0	
		Pt−O	0.2	2.05	0.001	−2.8	

surface alloy. For reduction at temperatures above about 400 °C, however, the surface CN_{Pt-Cr}/CN_{Pt-Pt} ratio of about 0.5 is consistent with the full monolayer coverage of Pt_3Cr.

The surface fits (Table 6) also show that the surface of $2Pt1Cr/SiO_2$ is more Pt rich than that of $2Pt3Cr/SiO_2$. For example, at 550 °C reduction, the CN_{Pt-Cr}/CN_{Pt-Pt} surface compositions are 0.40 and 0.55 in $2Pt1Cr/SiO_2$ and $2Pt3Cr/SiO_2$, respectively. For the former, even at 800 °C, the difference EXAFS indicates a surface with both monometallic Pt and Pt_3Cr in $2Pt1Cr/SiO_2$. The excess surface Pt explains why this catalyst has lower selectivity than that of $2Pt3Cr/SiO_2$. The CN_{Pt-Cr}/CN_{Pt-Pt} ratios for the reduced bimetallic Pt−Cr nanoparticles, oxidized bimetallic Pt−Cr nanoparticles, and surface of bimetallic Pt−Cr nanoparticles are given in Table 7.

Table 7. EXAFS Coordination Ratios for the Reduced Bimetallic Pt−Cr Nanoparticles (Average), Oxidized Bimetallic Pt−Cr Nanoparticles (Particle Interior), and Surface of Bimetallic Pt−Cr Nanoparticles

		CN_{Pt-Cr}/CN_{Pt-Pt}		
sample	reduction temperature (°C)	average	interior	surface
$2Pt1Cr/SiO_2$	550	0.28	0.25	0.40
	700	0.35	0.31	0.40
	800	0.38		
$2Pt3Cr/SiO_2$	250	0.16	0.11	0.31
	400	0.24	0.14	0.45
	550	0.30	0.22	0.56
	700	0.46	0.43	0.71
	800	0.52		

In $2Pt3Cr/SiO_2$, after reduction at 250 °C, the reduced particle has a CN_{Pt-Cr}/CN_{Pt-Pt} of 0.16, whereas the surface has 0.31. The particle interior has less Cr than the average composition. Thus, the initial Cr is formed at the particle surface. At 250 °C, the surface composition is not consistent with the full monolayer of Pt_3Cr (CN_{Pt-Cr}/CN_{Pt-Pt} = 0.5). Increasing the reduction temperature leads to an increase in the CN_{Pt-Cr}/CN_{Pt-Pt} ratios of the reduced nanoparticle (0.24) and surface (0.45). The particle interior is a mixture of Pt and Pt_3Cr, whereas the surface is nearly a complete Pt_3Cr monolayer. At higher reduction temperatures, the surface is little changed, whereas the Cr composition of the particle interior increases. Above about 700 °C, the nanoparticles are nearly a full Pt_3Cr alloy with little remaining monometallic Pt. At 700 °C, the surface EXAFS appears to be Cr rich compared with the Pt_3Cr alloy; however, as the particle size increase, the errors in the difference spectrum become less reliable.

In principle, the difference analysis can be applied to the XRD patterns. Direct oxidation of the surface leads to the formation of Pt−O and Cr−O, which are amorphous. Although the difference XRD patterns of catalysts reduced at low temperatures were narrower, more symmetric, and shifted slightly to a higher angle compared with the reduced pattern, it was not possible to resolve the surface structure due to the very similar peak positions of Pt and Pt_3Cr. For $2Pt3Cr/SiO_2$ reduced at 700 and 800 °C, where the peaks were larger and sharper, the difference XRD was possible. The small shifts in the difference XRD were consistent with only the Pt_3Cr phase at the surface (Figure 10). At these high reduction temperatures, the surface and average composition indicate the same Pt_3Cr structure.

The catalyst characterizations, e.g., fully reduced, oxidized, and surface, lead to a better understanding of the resulting structure of nanoparticles. Both the composition and reduction temperature affect the resulting structure and morphology (Figure 11). Although the metal oxides of Pt and Cr are deposited on the SiO_2 surface, the reduction of PtO_x is kinetically more favorable than that of Cr_2O_3; thus, Pt is initially reduced.[38−40] Pt activates H_2, reducing Cr_2O_3 at lower temperatures than in the absence of Pt.[41−44] Small amounts of metallic Cr are incorporated in the initially formed Pt nanoparticles as low as 250 °C. At this temperature, in $2Pt3Cr/SiO_2$, the average nanoparticle composition has 8 times more Pt than Cr. The surface analysis, however, indicates that the surface has more metallic Cr than the reduced nanoparticle but a full monolayer has not yet formed. In addition, the EXAFS of the particle interior shows little Cr. These analyses are consistent with a mechanism of alloy formation where catalytic reduction of nearby Cr_2O_3 leads to a

DOI: 10.1021/acs.chemmater.8b04774
Chem. Mater. 2019, 31, 1597−1609

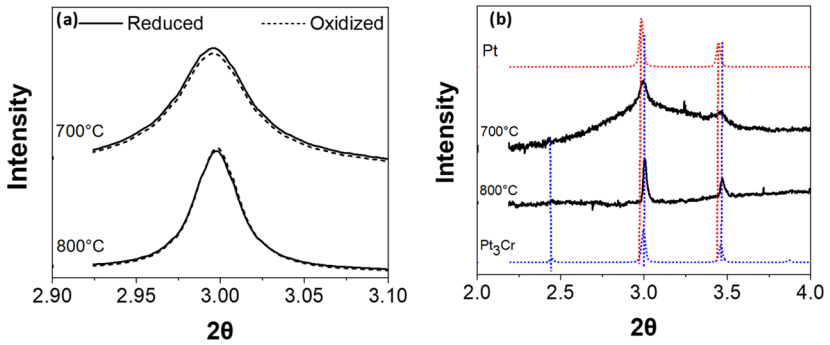

Figure 10. (A) Diffraction patterns for (111) and (200) peaks after the catalyst was reduced (solid) and oxidized (dashed). Pt and Pt_3Cr simulations at the appropriate lattice parameter of the reduced sample are provided for reference. (B) Difference XRD where the diffraction pattern of the oxidized sample is subtracted from that of the reduced.

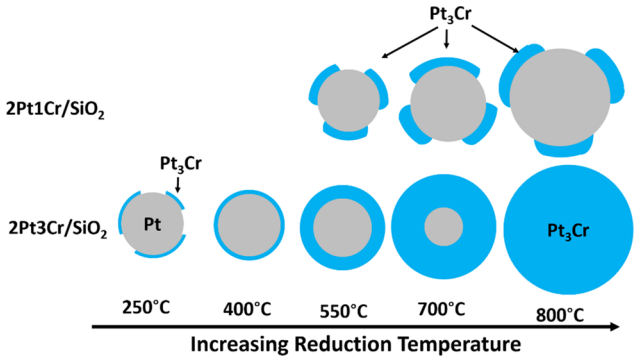

Figure 11. Cr incorporation into Pt nanoparticles in $2Pt1Cr/SiO_2$ and $2Pt3Cr/SiO_2$ with the increasing reduction temperature.

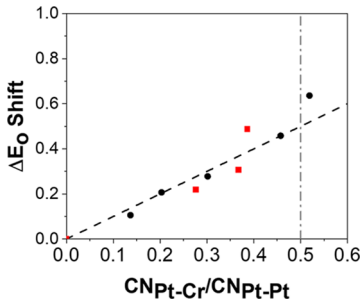

Figure 12. XANES energy shift for $2Pt1Cr/SiO_2$ (red) and $2Pt3Cr/SiO_2$ (black) as a function of the coordination number ratio, where the expected E_o shift (gray dot-dash) for Pt_3Cr phase occurs when CN_{Pt-Cr}/CN_{Pt-Pt} =0.5.

surface alloy.[43,45−47] This mechanism is consistent with that reported for a β_1-PdZn alloy.[31]

The amount of metallic Cr in the nanoparticle increases with the increasing reduction temperature, but the surface composition remains nearly constant with a structure consistent with Pt_3Cr. The additional Cr incorporation occurs in the subsurface of the nanoparticles. Cr diffusion continues at higher temperatures until a full Pt_3Cr intermetallic alloy is formed. To form a Pt_3Cr nanoparticle, only about 6% of Cr_2O_3 in $2Pt3Cr/SiO_2$ is reduced. Most of the Cr (>94%) remains oxidized in these samples, presumably the Cr oxide that is distant from the Pt nanoparticles. XAS analysis at the Cr K-edge was not able to detect the small fraction of metallic Cr. Although there is sufficient Cr in the catalyst to form bimetallic nanoparticles with higher content, due to the difficulty to reduce Cr oxide on SiO_2, Cr-rich phases (PtCr and $PtCr_3$) are not formed even after reduction at 800 °C.

At 1 wt % Cr loading, there is still a larger molar excess of Cr than is needed to form a surface alloy and even a full Pt_3Cr nanoparticle, but a full surface layer of Pt_3Cr does not form under any reduction condition. This suggests that there is insufficient CrO_x near the Pt nanoparticles.

As the amount of Cr increases, the shift in the XANES energy also increases proportional to the amount of Pt_3Cr in the nanoparticles, e.g., plotted as CN_{Pt-Cr}/CN_{Pt-Pt} (Figure 12). For Pt_3Cr, the ratio of 0.5 is a fully alloyed nanoparticle. By fitting the XANES spectra for any catalyst with the Pt and Pt_3Cr ($2Pt3Cr/SiO_2$ reduced at 800 °C) XANES, one can determine the fraction of each phase. This fraction can also be obtained using ratios of EXAFS coordination numbers.

With the fraction of each phase and the TEM particle size, the shell thickness can be approximated. For example, in $2Pt3Cr/SiO_2$, after reduction at 550 °C, CN_{Pt-Pt} is 8.1 and CN_{Pt-Cr} is 2.4. Since all Pt−Cr scattering is due to the formation of Pt_3Cr and the ratio of CN_{Pt-Pt} in the alloy is twice that for Pt−Cr, CN_{Pt-Pt} in the alloy fraction is 4.8, leaving CN_{Pt-Pt} = 3.3 in the core. These ratios indicate that about 60% (4.8/8.1) of Pt is present at Pt_3Cr and 40% is monometallic Pt. This can be visualized in the left part of Figure 13 for $2Pt3Cr/SiO_2$ after reduction at 550 °C, where the total particle size was 2.5 nm (TEM). Approximating nanoparticles as a sphere $\left(V = \frac{4}{3}\pi r^3\right)$, the ratio of the volume of the nanoparticle to the volume of a Pt_3Cr unit cell can be used to determine the number of atoms in the nanoparticle. Knowing the number of Pt−Pt and Pt−Cr bonds (EXAFS) in the nanoparticle allows for the determination of the inner Pt core size. By subtracting this from the total nanoparticle size, the shell thickness can be calculated.

For $2Pt_3Cr/SiO_2$ after reduction at 550 °C, the inner Pt core has a radius of approximately 1.0 nm and the shell is approximately 0.4 nm thick on either side of the core. The shell thickness estimates for the $2Pt3Cr/SiO_2$ catalyst at different reduction temperatures are given in Table 8. Similar calculations for $2Pt1Cr/SiO_2$ reduced at 550 °C give surface fractions of about 0.3 Pt and 0.7 Pt_3Cr. This model is based on the average (reduced) and surface compositions of the nanoparticles.

The two Pt−Cr bimetallic catalysts were very similar in terms of their bulk characterization after reduction at 550 °C. Both were bimetallic nanoparticles by XANES and EXAFS

DOI: 10.1021/acs.chemmater.8b04774
Chem. Mater. 2019, 31, 1597−1609

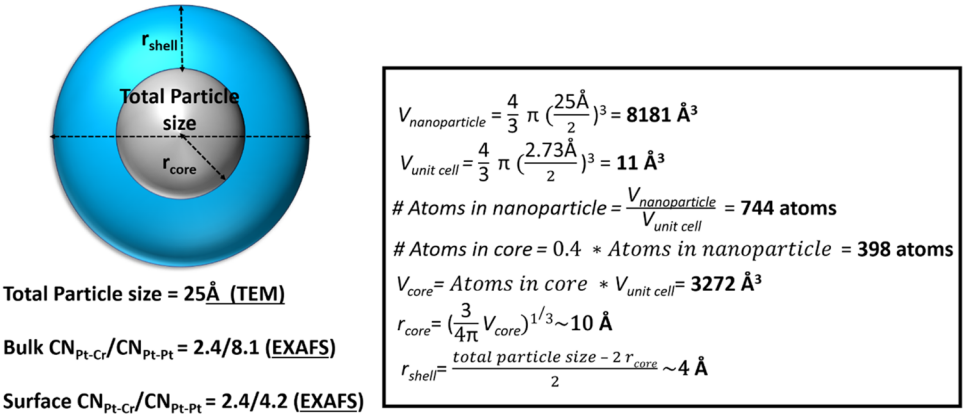

Figure 13. Sample calculation for shell thickness in Pt_3Cr@Pt core−shell nanoparticles after reduction at 550 °C.

Table 8. Fraction of Pt_3Cr in $2Pt3Cr/SiO_2$ and $2Pt1Cr/SiO_2$ as a Function of Reduction Temperature

sample	reduction temperature (°C)	fraction of Pt_3Cr (%)	r_{shell} (nm)	no. of atomic layers in Pt_3Cr shell
$2Pt1Cr/SiO_2$	550	37	0.2	0.8
	700	47	0.4	1.3
	800	51	0.5	1.7
$2Pt3Cr/SiO_2$	250	30	0.1	0.3
	400	42	0.2	0.6
	550	60	0.4	1.3
	700	91	1.0	3.7
	800	100	1.7	6.2

with similar changes in the XANES energy. The XRD patterns were also very similar. However, the EXAFS of the difference spectrum of $2Pt1Cr/SiO_2$ indicates that a full surface alloy is not formed and about 30% of the surface remains monometallic Pt. This correlates with the lower olefin selectivity (88%) compared with that of $2Pt3Cr/SiO_2$ (>97%), which forms a complete monolayer of a Pt_3Cr intermetallic alloy.

In summary, Pt_3Cr bimetallic nanoparticles were synthesized with different Cr loadings and evaluated for their catalytic performances for propane dehydrogenation. Although characterization methods of the average structure suggested similar morphologies, higher Cr loading displayed higher olefin selectivity. Small changes in surface composition were only observed using difference XAS and XRD, which showed that the morphology of the catalyst changes with the Cr content and reduction temperature. The best catalytic performance was observed in nanoparticles containing at least a full Pt_3Cr surface alloy.

CONCLUSIONS

Confirmation of the Pt_3Cr structure in these bimetallic catalysts is not enough to understand their catalytic performances since several structures and morphologies are possible. In this study, Pt−Cr alloys containing varying amounts of Cr were prepared at increasing reduction temperatures. Although reduction at high temperatures and higher Cr loading led to the formation of a full Pt_3Cr alloy, Pt core with Pt_3Cr shell nanoparticles were formed at lower temperatures. At lower Cr loadings, there was insufficient Cr_2O_3 near Pt nanoparticles to form a complete surface alloy. However, the addition of even small amounts of Cr led to improvements in olefin selectivity for propane dehydrogenation compared with that of monometallic Pt.

While XAS and XRD confirm the presence of bimetallic nanoparticles with a two-phase composition (Pt and Pt_3Cr), these are insufficient to determine the structure of the catalytic surface. By analysis of the oxidized catalysts, the structure of the particle interior could be determined. The difference spectrum of reduced and oxidized catalysts also allowed for the determination of the surface composition and structure. The nanoparticles were shown to contain more Cr at the surface than at the interior. In addition, from the surface XAS and XRD, the specific intermetallic Pt_3Cr phase was more easily identified than in the fully reduced, two-phase (Pt + Pt_3Cr) nanoparticles. Utilizing these analyses along with the TEM particle size also allows for the determination of the shell thickness in core−shell bimetallic nanoparticles.

AUTHOR INFORMATION

Corresponding Authors

*E-mail: gzhang@dlut.edu.cn (G.Z.).
*E-mail: mill1194@purdue.edu (J.T.M.).

ORCID

Guanghui Zhang: 0000-0002-5854-6909
Jeffrey T. Miller: 0000-0002-6269-0620

Notes

The authors declare no competing financial interest.

ACKNOWLEDGMENTS

N.J.L., G.Z., and J.T.M. were supported in part by the National Science Foundation under Cooperative Agreement no. EEC-1647722. G.Z. would also like to acknowledge the Fundamental Research Funds for the Central Universities (DUT18RC(3)057). Use of the Center for Nanoscale Materials and Advanced Photon Source, both Office of Science user facilities, was supported by the U.S. Department of Energy, Office of Science, Office of Basic Energy Sciences, under Contract No. DE-AC02-06CH11357. MRCAT operations and the beamline 10-BM were supported by the Department of Energy and the MRCAT member institutions. The authors also acknowledge the use of the beamline 11-ID-C.

REFERENCES

(1) Singh, A. K.; Xu, Q. Synergistic Catalysis over Bimetallic Alloy Nanoparticles. *ChemCatChem* **2013**, *5*, 652−676.

DOI: 10.1021/acs.chemmater.8b04774
Chem. Mater. 2019, 31, 1597−1609

(2) Chen, T.; Rodionov, V. O. Controllable Catalysis with Nanoparticles: Bimetallic Alloy Systems and Surface Adsorbates. *ACS Catal.* **2016**, *6*, 4025−4033.
(3) Louis, C. Chemical Preparation of Supported Bimetallic Catalysts. Gold-Based Bimetallic, a Case Study. *Catalysts* **2016**, *6*, No. 110.
(4) Sattler, J. J.; Ruiz-Martinez, J.; Santillan-Jimenez, E.; Weckhuysen, B. M. Catalytic Dehydrogenation of Light Alkanes on Metals and Metal Oxides. *Chem. Rev.* **2014**, *114*, 16013−16063.
(5) Sinfelt, J. H. Catalysis by Alloys and Bimetallic Clusters. *Acc. Chem. Res.* **1977**, *10*, 15−20.
(6) Wong, A.; Liu, Q.; Griffin, S.; Nicholls, A.; Regalbuto, J. R. Synthesis of ultrasmall, homogeneously alloyed, bimetallic nanoparticles on silica supports. *Science* **2017**, *358*, 1427−1430.
(7) Furukawa, S.; Komatsu, T. Intermetallic Compounds: Promising Inorganic Materials for Well-Structured and Electronically Modified Reaction Environments for Efficient Catalysis. *ACS Catal.* **2017**, *7*, 735−765.
(8) Wu, Z.; Wegener, E. C.; Tseng, H.; Gallagher, J. R.; Harris, J. W.; Diaz, R. E.; Ren, Y.; Ribeiro, F. H.; Miller, J. T. Pd−In intermetallic alloy nanoparticles: highly selective ethane dehydrogenation catalysts. *Catal. Sci. Technol.* **2016**, *6*, 6965−6976.
(9) Ma, Z.; Wu, Z.; Miller, J. T. Effect of Cu content on the bimetallic Pt−Cu catalysts for propane dehydrogenation. *Catal., Struct. React.* **2017**, *3*, 43−53.
(10) Alexeev, O. S.; Gates, B. C. Supported Bimetallic Cluster Catalysts. *Ind. Eng. Chem. Res.* **2003**, *42*, 1571−1587.
(11) Bugaev, A. L.; Guda, A. A.; Lomachenko, K. A.; Shapovalov, V. V.; Lazzarini, A.; Vitillo, J. G.; Bugaev, L. A.; Groppo, E.; Pellegrini, R.; Soldatov, A. V.; van Bokhoven, J. A.; Lamberti, C. Core−Shell Structure of Palladium Hydride Nanoparticles Revealed by Combined X-ray Absorption Spectroscopy and X-ray Diffraction. *J. Phys. Chem. C* **2017**, *121*, 18202−18213.
(12) Bugaev, A. L.; Guda, A. A.; Lomachenko, K. A.; Srabionyan, V. V.; Bugaev, L. A.; Soldatov, A. V.; Lamberti, C.; Dmitriev, V. P.; van Bokhoven, J. A. Temperature- and Pressure-Dependent Hydrogen Concentration in Supported PdHx Nanoparticles by Pd K-Edge X-ray Absorption Spectroscopy. *J. Phys. Chem. C* **2014**, *118*, 10416−10423.
(13) Gallagher, J. R.; Childers, D. J.; Zhao, H.; Winans, R. E.; Meyer, R. J.; Miller, J. T. Structural evolution of an intermetallic Pd−Zn catalyst selective for propane dehydrogenation. *J. Phys. Chem. A* **2015**, *17*, 28144−28153.
(14) Yang, C.; Wu, Z.; Zhang, G.; Sheng, H.; Tian, J.; Duan, Z.; Sohn, H.; Kropf, J. A.; Wu, T.; Krause, T. R.; Miller, J. T. Promotion of Pd nanoparticles by Fe and formation of a Pd3Fe intermetallic alloy for propane dehydrogenation. *Catal. Today* **2019**, *323*, 123−128.
(15) Ye, C.; Wu, Z.; Liu, W.; Ren, Y.; Zhang, G.; Miller, J. T. Structure Determination of a Surface Tetragonal Pt1Sb1 Phase on Pt Nanoparticles. *Chem. Mater.* **2018**, *30*, 4503−4507.
(16) Wegener, E. C.; Wu, Z.; Tseng, H.; Gallagher, J. R.; Ren, Y.; Diaz, R. E.; Ribeiro, F. H.; Miller, J. T. Structure and reactivity of Pt−In intermetallic alloy nanoparticles: Highly selective catalysts for ethane dehydrogenation. *Catal. Today* **2017**, *299*, 146−153.
(17) Childers, D. J.; Schweitzer, N. M.; Shahari, S. M. K.; Rioux, R. M.; Miller, J. T.; Meyer, R. J. Modifying structure-sensitive reactions by addition of Zn to Pd. *J. Catal.* **2014**, *318*, 75−84.
(18) Wanjala, B. N.; Luo, J.; Loukrakpam, R.; Fang, B.; Mott, D.; Njoki, P. N.; Engelbard, M.; Naslund, R. H.; Wu, J. K.; Wang, L.; Malis, O.; Zhong, C. J. Nanoscale Alloying, Phase-Segregation, and Core−Shell Evolution of Gold−Platinum Nanoparticles and Their Electrocatalytic Effect on Oxygen Reduction Reaction. *Chem. Mater.* **2010**, *22*, 4282−4294.
(19) Wu, Z.; Bukowski, B. C.; Li, Z.; Milligan, C.; Zhou, L.; Ma, T.; Wu, Y.; Ren, Y.; Ribeiro, F. H.; Delgass, N. W.; Greeley, J. P.; Zhang, G.; Miller, J. T. Changes in Catalytic and Adsorptive Properties of 2 nm Pt3Mn Nanoparticles by Subsurface Atoms. *J. Am. Chem. Soc.* **2018**, *140*, 14870−14877.
(20) Tao, F.; Grass, M. E.; Zhang, Y.; Butcher, D. R.; Renzas, J. R.; Liu, Z.; Chung, J. Y.; Mun, B. S.; Salmerson, M.; Somojai, G. A. Reaction-Driven Restructuring of Rh-Pd and Pt-Pd Core-Shell Nanoparticles. *Science* **2008**, *322*, 932−934.
(21) Cai, Z.; Chattopadhyay, N.; Liu, W. J.; Chan, C.; Pignol, J. P.; Reilly, R. M. Optimized digital counting colonies of clonogenic assays using ImageJ software and customized macros: Comparison with manual counting. *Int. J. Radiat. Biol.* **2011**, *87*, 1135−1146.
(22) Yoshida, H.; Omote, H.; Takeda, S. Oxidation and reduction processes of platinum nanoparticles observed at the atomic scale by environmental transmission electron microscopy. *Nanoscale* **2014**, *6*, 13113−13118.
(23) Ressler, T. WinXAS: a Program for X-ray Absorption Spectroscopy Data Analysis under MS-Windows. *J. Synchrotron Radiat.* **1998**, *5*, 118−122.
(24) Rehr, J. J.; Booth, C. H.; Bridges, F.; Zabinsky, S. I. X-ray-absorption fine structure in embedded atoms. *Phys. Rev. B* **1994**, *49*, 12347−12350.
(25) Hammersley, A. P.; Svensson, S. O.; Hanfland, M.; Fitch, A. N.; Hausermann, D. Two-dimensional detector software: From real detector to idealised image or two-theta scan: High Pressure Research. *High Pressure Res.* **1996**, *14*, 235−248.
(26) Chateigner, D.; Modreanu, M.; Murtagh, M. E.; Ricote, J.; Schreiber, J. In *Thin Solid Films*, Proceedings of Symposium M on Optical and X-Ray Metrology for Advanced Device Materials Characterization, 2004; Vol. *450*, pp 34−41.
(27) Hejral, U.; Muller, P.; Shiplin, M.; Gustafson, J.; Franz, D.; Shayduk, R.; Rutt, U.; Zhang, C.; Merte, L. R.; Lundgren, E.; Vonk, V.; Stierle, A. High-energy x-ray diffraction from surfaces and nanoparticles. *Phys. Rev. B* **2017**, *96*, No. 195433.
(28) Leontyev, I. N.; Kuriganova, A. B.; Leontyev, N. G.; Hennet, L.; Rakhmatullin, A.; Smirnova, N. V.; Dmitriev, V. Size dependence of the lattice parameters of carbon supported platinum nanoparticles: X-ray diffraction analysis and theoretical considerations. *RSC Adv.* **2014**, *4*, 35959−35965.
(29) Yang, W.; Zou, L.; Huang, Q.; Zou, Z.; Hu, Y.; Yang, H. Lattice Contracted Ordered Intermetallic Core-Shell PtCo@Pt Nanoparticles: Synthesis, Structure and Origin for Enhanced Oxygen Reduction Reaction. *J. Electrochem. Soc.* **2017**, *164*, H331−H337.
(30) Okamoto, H. *Phase Diagrams for Binary Alloys*; ASM International: Materials Park, OH, 2010.
(31) Antolini, E.; Salgado, J. R. C.; Santos, L. G. R. A.; et al. Carbon supported Pt-Cr alloys as oxygen-reduction catalysts for direct methanol fuel cells. *J. Appl. Electrochem.* **2006**, *36*, 355−362.
(32) Lei, Y.; Jelic, J.; Nitsche, L. C.; Meyer, R.; Miller, J. T. Effect of Particle Size and Adsorbates on the L3, L2 and L1 X-ray Absorption Near Edge Structure of Supported Pt Nanoparticles. *Top. Catal.* **2011**, *54*, 334−348.
(33) Chakrabarti, A.; Wachs, I. E. The Nature of Surface CrOx Sites on SiO2 in Different Environments. *Catal. Lett.* **2015**, *145*, 985−994.
(34) Delley, M. F.; Conley, M. P.; Copéret, C. Polymerization on CO-Reduced Phillips Catalyst initiates through the C−H bond Activation of Ethylene on Cr−O Sites. *Catal. Lett.* **2014**, *144*, 805−808.
(35) Conley, M. P.; Delley, M. F.; Núñez-Zarur, F.; Comas-Vives, A.; Copéret, C. Heterolytic Activation of C-H Bonds on Cr(III)-O Surface Sites Is a Key Step in Catalytic Polymerization of Ethylene and Dehydrogenation of Propane. *Inorg. Chem.* **2015**, *54*, 5065−5078.
(36) Cui, Z.; Chen, H.; Zhou, W.; Zhao, M.; DiSalvo, F. J. Structurally Ordered Pt3Cr as Oxygen Reduction Electrocatalyst: Ordering Control and Origin of Enhanced Stability. *Chem. Mater.* **2015**, *27*, 7538−7545.
(37) Gallagher, J. R.; Li, T.; Zhao, H.; Liu, J.; Lei, Y.; Zhang, X.; Ren, Y.; Elam, J. W.; Meyer, R. J.; Winans, R. E.; Miller, J. T. In situ diffraction of highly dispersed supported platinum nanoparticles. *Catal. Sci. Technol.* **2014**, *4*, 3053−3063.
(38) Anderson, J. R. *Structure of Metallic Catalysts*; Academic Press: New York, NY, 1975.
(39) Klissurski, D.; Dimitrova, R. Reducibility of Metal Oxides in Hydrogen and Strength of Oxygen Bond in Their Surface Layer. *Bull. Chem. Soc. Jpn.* **1990**, *63*, 590−591.

DOI: 10.1021/acs.chemmater.8b04774
Chem. Mater. 2019, 31, 1597−1609

(40) Fang, Z.; Vasiliu, M.; Peterson, K. A.; Dixon, D. A. Prediction of Bond Dissociation Energies/Heats of Formation for Diatomic Transition Metal Compounds: CCSD(T) Works. *J. Chem. Theory Comput.* **2017**, *13*, 1057−1066.
(41) Bond, G. C.; Tripathi, J. B. P. Studies of hydrogen spillover. Part 3.—Catalysis of the reduction of metal oxides by palladium on silica. *J. Chem. Soc., Faraday Trans. 1* **1976**, *72*, 933−941.
(42) Karim, W.; Spreafico, C.; Kleibert, A.; Gobrecht, J.; VandeVondele, J.; Ekinci, Y.; van Bokhoven, J. A. Catalyst support effects on hydrogen spillover. *Nature* **2017**, *541*, 68−71.
(43) Tew, M. W.; Emerich, H.; van Bokhoven, J. A. Formation and Characterization of PdZn Alloy: A Very Selective Catalyst for Alkyne Semihydrogenation. *J. Phys. Chem. C* **2011**, *115*, 8457−8465.
(44) Choi, M.; Yook, S.; Kim, H. Hydrogen Spillover in Encapsulated Metal Catalysts: New Opportunities for Designing Advanced Hydroprocessing Catalysts. *ChemCatChem* **2015**, *7*, 1048−1057.
(45) Föttinger, K.; van Bokhoven, J. A.; Nachtegaal, M.; Rupprechter, G. Dynamic Structure of a Working Methanol Steam Reforming Catalyst: In Situ Quick-EXAFS on Pd/ZnO Nanoparticles. *J. Phys. Chem. Lett.* **2011**, *2*, 428−433.
(46) Pham, H. N.; Sattler, J. J.; Weckhuysen, B. M.; Datye, A. K. Role of Sn in the Regeneration of Pt/γ-Al2O3 Light Alkane Dehydrogenation Catalysts. *ACS Catal.* **2016**, *6*, 2257−2264.
(47) Cortright, R. D.; Hill, J. M.; Dumesic, J. A. Selective dehydrogenation of isobutane over supported Pt/Sn catalysts. *Catal. Today* **2000**, *55*, 213−223.

DOI: 10.1021/acs.chemmater.8b04774
Chem. Mater. 2019, 31, 1597−1609